Title

Understanding the Fluorination of Disordered Rocksalt Cathodes through Rational Exploration of Synthesis Pathways

Journal

Chemistry of Materials, 34(15)

ISSN

0897-4756

Authors

Szymanski, Nathan J

Zeng, Yan

Bennett, Tyler

et al.

Publication Date

2022-08-09

DOI

10.1021/acs.chemmater.2c01474

Understanding the fluorination of disordered rocksalt cathodes through rational exploration of synthesis pathways

Nathan J. Szymanski[1,2,*], Yan Zeng[2,*], Tyler Bennett[3], Shripad Patil[3,4], Jong K. Keum[5], Ethan C. Self[3], Jianming Bai[6], Zijian Cai[1,2], Raynald Giovine[7,8], Bin Ouyang[1,2], Feng Wang[9], Christopher J. Bartel[1,2], Raphaële J. Clément[7], Wei Tong[10], Jagjit Nanda[3], and Gerbrand Ceder[1,2,†]

[1]Department of Materials Science & Engineering, UC Berkeley, Berkeley, CA 94720, USA
[2]Materials Sciences Division, Lawrence Berkeley National Laboratory, Berkeley, CA 94720, USA
[3]Chemical Sciences Division, Oak Ridge National Laboratory, Oak Ridge, TN 37830, USA
[4]Bredesen Center for Interdisciplinary Research and Graduate Education, University of Tennessee Knoxville, Knoxville, TN, 37996, USA
[5]Center for Nanophase Materials Sciences and Neutron Scattering Division, Oak Ridge National Laboratory, Oak Ridge, TN 37830, USA
[6]National Synchrotron Light Source II, Brookhaven National Laboratory, Upton, NY 11973, USA
[7]Materials Department, UC Santa Barbara, Santa Barbara, CA 93106, USA
[8]Materials Research Laboratory, UC Santa Barbara, Santa Barbara, CA 93106, USA
[9]Energy & Photon Science Directorate, Brookhaven National Laboratory, Upton, NY 11973, USA
[10]Energy Storage and Distributed Resources Division, Lawrence Berkeley National Laboratory, Berkeley, CA 94720, USA
[*]Authors contributed equally
[†]Corresponding author, gceder@berkeley.edu

Abstract

We have designed and tested several synthesis routes targeting a highly fluorinated disordered rocksalt (DRX) cathode, $Li_{1.2}Mn_{0.4}Ti_{0.4}O_{1.6}F_{0.4}$, with each route rationalized by thermochemical analysis. Precursor combinations were screened to raise the F chemical potential and avoid the formation of LiF, which inhibits fluorination of the targeted DRX phase. MnF_2 was used as a reactive source of F, and Li_6MnO_4, $LiMnO_2$, and $Li_2Mn_{0.33}Ti_{0.66}O_3$ were tested as alternative Li sources. Each synthesis procedure was monitored using a multi-modal suite of characterization techniques including X-ray diffraction, nuclear magnetic resonance, thermogravimetric analysis, and differential scanning calorimetry. From the resulting data, we advance the understanding of oxyfluoride synthesis by outlining the key factors limiting F solubility. At low temperatures, MnF_2 consistently reacts with the Li source to form LiF as an intermediate phase, thereby trapping F in strong Li-F bonds. LiF can react with Li_2TiO_3 to form a highly lithiated and fluorinated DRX (Li_3TiO_3F); however, MnO is not easily incorporated into this DRX phase. Although higher temperatures typically increase solubility, the volatility of LiF above its melting point (848 °C) inhibits fluorination of the DRX phase. Based on these findings, metastable synthesis techniques are suggested for future work on DRX fluorination.

Introduction

The development of improved Li-ion batteries is essential to meet the growing demand for energy storage. Cation-disordered rocksalt (DRX) materials are a promising class of cathodes with high energy densities that can exceed traditional layered cathodes such as $LiCoO_2$ and $Li(Ni, Mn, Co)O_2$ (NMC) without requiring the use of Ni or Co [1]. In contrast to the ordered structure of layered oxides, DRX materials are characterized by disordered Li and transition metal ions within the face-centered cubic oxygen lattice, where facile Li diffusion can occur across a network of tetrahedral sites with low energy barriers [2, 3]. The disordered cation sublattice can host a variety of elements, creating the opportunity to use low-cost, redox-active transition metals such as Mn or Fe [4-6]. Ionic substitution can also be carried out on the O sublattice; in particular, fluorination has been used to raise the capacity and improve the cyclability of DRX cathodes [7-11]. Recent work on Mn/Nb-based DRX oxyfluorides demonstrated that capacity retention improves upon increasing substitution of O with F, suggesting that maximal fluorination is key to optimizing performance [12, 13].

DRX oxyfluorides are conventionally made by solid-state synthesis with LiF as the single source of F. Because LiF contains highly ionic Li-F bonds with a large dissociation energy, the solubility limit between LiF and most lithium transition metal oxides is low. For DRX oxyfluorides with a composition of $Li_{1.2}(Mn/Ti)_{0.8}O_{2-x}F_x$, first-principles calculations indicate that only 5% O/F substitution ($x \leq 0.1$) can be achieved at a synthesis temperature of 1000 ℃ [14]. The solubility limit can be slightly improved for other compositions (e.g., through Mn/Ni replacement or increased Li content), but generally remains below 10%. In the place of traditional solid-state synthesis, high-energy ball milling can be used to increase F uptake into DRX materials [7, 15]. However, this method is not easily scalable as it requires high energy input and produces small sample quantities per batch [16]. Moreover, ball milling reduces particle size and therefore cannot be used to make larger (e.g., micron-sized) particles that are sometimes desired for battery materials [17]. Alternatively, organic fluoropolymers (e.g., PTFE) can be used as precursors for DRX oxyfluoride synthesis, potentially leading to higher F content in the final products than those synthesized using LiF [18]. Despite this improvement, the volatility of such fluorinating agents at moderate temperature (350 ℃ for PTFE) can be problematic, and LiF still appears as a secondary phase when attempting to make DRX compositions with greater than 10% O/F substitution.

In this work, we evaluate several new synthesis routes targeting $Li_{1.2}Mn_{0.4}Ti_{0.4}O_{1.6}F_{0.4}$, and in the process clarify the specific reaction pathways that make high F uptake so challenging. $Li_{1.2}Mn_{0.4}Ti_{0.4}O_{1.6}F_{0.4}$ has a high theoretical TM capacity (~260 mAh/g from $Mn^{2+/4+}$ redox), made possible by a substantial amount of O/F substitution (20%) that is well beyond the equilibrium solubility limit (5%) at 1000 ℃ [14]. Precursor sets were designed by optimizing the F chemical potential, maximizing the driving force to form the DRX phase, and minimizing the driving force to form any competing phases. MnF_2 is identified as a promising fluorination agent owing to its high F chemical potential, well exceeding that of LiF. However, we postulate that MnF_2 can improve F solubility only if it directly contributes to DRX formation rather than forming LiF as an intermediate phase, which would otherwise trap all F ions in strong Li-F bonds and lower the F chemical potential. Accordingly, several lithium metal oxides were tested as precursors to "lock in" Li and avoid LiF formation. Syntheses were monitored *in situ* using X-ray diffraction (XRD), thermogravimetric analysis (TGA), and differential scanning calorimetry (DSC). Nuclear magnetic resonance (NMR) was also applied *ex situ* to characterize the synthesis products. Through a detailed analysis of the observed reaction pathways, we pinpoint several factors governing the synthesis of DRX oxyfluorides.

Methods

Thermochemical data

Formation energies calculated by density functional theory (DFT) were extracted from the Materials Project [19] for all available entries in the Li-Mn-Ti-O-F chemical space, also including carbonates. These DFT-calculated energies describe the materials at 0 K and therefore do not include any finite temperature effects (e.g., vibrational or configurational entropy). We estimated the temperature dependent Gibbs free energies for all solid phases using the machine-learned descriptor developed by Bartel *et al.* [20], which can accurately model the effects of vibrational entropy. Except for the DRX phase, all materials are assumed to be ordered and therefore configurational entropy effects are neglected. For any gaseous species (O_2, CO_2, and CO) considered as possible reaction byproducts, free energies were calculated by summing DFT-calculated energies from the Materials Project with temperature dependent experimental corrections from the NIST database [21]. For both solid and gaseous phases, Gibbs free energies were calculated at 800 ℃, a temperature commonly used for solid-state synthesis. A low partial

pressure of 0.1 Pa was assumed for O_2, CO_2, and CO as all syntheses considered here are carried out under an Ar atmosphere. Reaction energies were calculated as the difference between the Gibbs free energy of the products and the reactants at 800 ℃, normalized per atom of the product phase(s) formed.

To account for the impact of configurational entropy on the free energy of the targeted DRX phase, $Li_{1.2}Mn_{0.4}Ti_{0.4}O_{1.6}F_{0.4}$, we constructed a cluster-expansion Hamiltonian on the octahedral cation and anion sites of the rocksalt structure, following a similar procedure described in previous work [14]. Pair interactions up to 7.1 Å, triplet interactions up to 4.0 Å, and quadruplet interactions up to 4.0 Å were included in the cluster-expansion formalism. All interactions were taken with respect to a baseline screened electrostatic energy defined by the formal charges of the ionic species (Li^+, Mn^{2+}, Ti^{4+}, O^{2-}, and F^-). The effective cluster interaction (ECI) coefficients were fitted to DFT-calculated energies using an L_1-regularized least-squares regression approach designed to minimize the cross-validation error [22]. Based on a fitting of energies from 653 distinct structures, we obtained a cross-validation error of 7 meV/atom. Canonical Monte Carlo simulations were carried out to obtain the internal energy of $Li_{1.2}Mn_{0.4}Ti_{0.4}O_{1.6}F_{0.4}$ as a function of temperature, from which the Gibbs free energy was calculated by integrating the heat capacity [23].

Our cluster-expansion calculations reveal that $Li_{1.2}Mn_{0.4}Ti_{0.4}O_{1.6}F_{0.4}$ is metastable with respect to phase segregation into Li_2TiO_3, MnO, and LiF. Based on the equilibrium phase diagram from Materials Project, the targeted DRX phase has an energy that is 25.3 meV/atom above the convex hull at 800 °C. This finding confirms recent reports that DRX materials generally have limited F solubility under equilibrium conditions and are therefore difficult to prepare using traditional solid-state synthesis [13, 14]. Nevertheless, several *in situ* studies have demonstrated that metastable intermediate phases can form during solid-state reactions when highly reactive precursors are used [24, 25]. Accordingly, we dedicate the next section to the identification of precursors that may lead to the formation of this metastable DRX phase ($Li_{1.2}Mn_{0.4}Ti_{0.4}O_{1.6}F_{0.4}$) with enhanced F solubility.

Precursor screening

Our objective is to design new synthesis routes for DRX oxyfluorides by choosing alternative precursors that lead to enhanced F solubility. From equilibrium thermodynamics, the solubility

limit of a particular species (i) in a host material occurs at the composition where the chemical potential of that species (μ_i) is equal between the host and any competing phase(s) [26]. When μ_i is lower (i.e., more negative) in the competing phases than in the host, the system can lower its energy by placing species *i* in those phases rather than the host material, thereby reducing the solubility of *i* in the host. With respect to DRX oxyfluorides, LiF is the competing phase that limits F solubility [14, 23] owing to its large formation energy ($E_{\mathrm{F}} \approx -3.18$ eV/atom) relative to Li and F_2 [19]. Because LiF remains stable at very low F chemical potential ($\mu_{\mathrm{F}} \geq -6.36$ eV), it inhibits the fluorination of DRX materials when used as the only F source. Accordingly, to enhance F solubility, we only considered more reactive precursor sets with $\mu_{\mathrm{F}} > -6.36$ eV. These include transition metal fluorides that may replace or be used in conjunction with LiF, as many fluoride mixtures are expected to form molten phases above their respective eutectic temperatures [27]. In **Supplementary Figure S1**, we show how the use of transition metal fluorides leads to increased μ_{F} relative to LiF.

Choosing starting materials with high μ_{F} is a necessary, though insufficient, condition to enhance F solubility in the final synthesis product. An additional requirement is to maintain high μ_{F} across any intermediate phases that form before the targeted DRX phase, as solid-state reactions often go through a series of intermediate phases before forming the final product(s) [24, 28]. Following this principle, LiF formation should be avoided if F solubility is to be improved. Our precursor search is therefore augmented with a second constraint that the thermodynamic driving force to form LiF from the starting materials is relatively weak. For each set, we identified the precursor pair with the largest (most negative) driving force ($\Delta \mathrm{G}$) to form LiF; if $\Delta \mathrm{G} < -250$ meV/atom of product(s) formed, then that set is excluded from further consideration. This cutoff was chosen such that each precursor set is less likely to form LiF than the interfacial reaction between MnF_2 and Li_2O ($\Delta \mathrm{G} \approx -255$ meV/atom). As will be demonstrated by our experimental results, avoiding a reaction between MnF_2 and the Li-containing oxide is critical to maintaining high μ_{F}.

To screen precursors for $Li_{1.2}Mn_{0.4}Ti_{0.4}O_{1.6}F_{0.4}$ in a high-throughput fashion, we parsed the Materials Project and obtained all reported entries in the Li-Mn-Ti-O-F chemical space [19]. Carbonates of each cation and elemental C were also considered. The resulting dataset contains 1,165 distinct phases. For practical purposes, any precursors used should be readily available or experimentally synthesizable through a standard and scalable technique. To satisfy this constraint,

we filtered all materials by two criteria: (1) each phase must have been previously reported in the ICSD [29], and (2) each phase must be synthesizable by a conventional solid-state route, as reported in the SynTERRA text-mined database and manually verified [30]. After applying both filters, the initial set of 1,165 materials was significantly reduced to 32 experimentally accessible phases that were used as a basis to form possible precursor sets for DRX synthesis. The number of precursors in each set was limited to ≤ 5 as this is the maximum number of phases that can be in equilibrium with one another in a five-component (Li-Mn-Ti-O-F) system according to the Gibbs phase rule [26]. Precursor sets that cannot be stoichiometrically balanced to yield $Li_{1.2}Mn_{0.4}Ti_{0.4}O_{1.6}F_{0.4}$ were excluded, allowing for gaseous byproducts including O_2, CO_2, and CO. These criteria produced a final list of 341 precursor sets that were considered promising for DRX oxyfluoride synthesis.

Results

Conventional precursors

To understand why highly fluorinated DRX cathodes are difficult to make using a conventional solid-state synthesis route, we first study the reaction pathway based on a standard mixture of LiF, TiO_2, Li_2CO_3, and MnO. In **Figure 1a**, XRD patterns are displayed for the synthesis products of these precursors when held at three different temperatures for one hour: 700, 850, and 1000 ℃. XRD from a fourth sample is also shown after a longer hold time of 12 hours at 1000 ℃. The results show that a DRX phase is formed by 700 ℃, at which point there are no detectable diffraction peaks from Li_2CO_3 or TiO_2, and very little signal from LiF. However, in addition to the DRX phase, intense MnO peaks remain apparent. This suggests that the MnO precursor has not yet reacted, leaving the DRX phase deficient in Mn. Assuming all other precursors are fully consumed to produce the DRX phase at 700 ℃, the nominal composition of this phase is Li_3TiO_3F. By refining each set of peaks based on a two-phase mixture of Li_3TiO_3F and MnO, we estimate that MnO has a weight fraction of about 26.3%, which is lower than its expected amount based on the stoichiometry of the starting mixture (34.3%). Hence, the DRX phase likely contains some Mn, but much less than in the targeted composition of $Li_{1.2}Mn_{0.4}Ti_{0.4}O_{1.6}F_{0.4}$ as most of the MnO precursor remains unreacted.

Upon heating the precursors to 850 ℃, a clear change appears in the XRD pattern of the corresponding products. The diffraction peaks from MnO are diminished while the LiF peaks

grow, suggesting that higher temperatures increase the amount of MnO incorporated into the DRX phase but also extract LiF from it. This conclusion is further evidenced by a change in the DRX peak positions. The (002) peak exhibits a 0.5° shift toward lower 2θ, indicating a lattice constant increase of ~1.2% caused by the addition of Mn^{2+} ions (85 pm radius) and the loss of Li^{+} ions (76 pm radius). This trend continues upon further heating to 1000 ℃. The LiF signal becomes more intense while the MnO signal is reduced to nearly zero. The DRX lattice constant also increases by an additional 0.3% relative to 850 ℃. Interestingly, when the sample is held at 1000 ℃ for 12 hours, the LiF peaks completely disappear. This leaves a pure DRX pattern that may lead one to believe that $Li_{1.2}Mn_{0.4}Ti_{0.4}O_{1.6}F_{0.4}$ was successfully made. However, the positions of the DRX peaks show only small changes (< 0.1°) relative to the sample synthesized using a one-hour hold time at 1000 ℃. We therefore suspect that LiF may not have been fully incorporated into the DRX phase, warranting further investigation by additional characterization techniques.

To gain insight into the behavior of LiF at high temperatures, we carried out TGA/DSC measurements on a sample of LiF held at 1000 ℃ for five hours. In **Figure 1b**, the corresponding mass loss and heat flow curves are shown. A critical feature is identified at 848 ℃, where an endothermic process occurs in accordance with the melting point of LiF [31]. Immediately above 848 ℃, the mass of the sample begins to decrease. Mass loss continues to occur as the sample is heated to 1000 ℃. After five hours at this temperature, only 35% of the starting mass remains. These findings reveal that LiF becomes volatile above its melting point when placed under flowing Ar, a necessary condition to avoid unwanted oxidation during the synthesis of Mn^{2+}-containing materials. We conclude that the DRX sample synthesized at 1000 ℃ appears pure not because LiF was successfully incorporated, but instead because LiF evaporated from the system.

To verify the absence of LiF in the sample synthesized at 1000 ℃ for 12 hours, NMR measurements were carried out on the corresponding product. In **Figure 1c**, we show the ^{19}F NMR spectrum measured from this sample, as well as a reference spectrum for LiF. Indeed, no LiF peak is found in the NMR spectrum ($\delta_{iso} = -204$ ppm) from the product synthesized from conventional precursors. Furthermore, the signal-to-noise ratio in the ^{19}F NMR of our synthesis product is much lower than typically observed for DRX materials with nominally high F content [13, 32, 33], synthesized by ball milling rather than by a traditional solid-state method. These findings support our conclusion that LiF is absent from the sample and that the synthesized DRX

composition likely contains very little F because most of the LiF precursor evaporated during synthesis.

Our synthesis data illustrates that the targeted composition, $Li_{1.2}Mn_{0.4}Ti_{0.4}O_{1.6}F_{0.4}$, was not successfully obtained at any point during the heating process when using conventional precursors (LiF, TiO_2, Li_2CO_3, and MnO). Despite this finding, a highly fluorinated DRX phase with a nominal composition of Li_3TiO_3F was identified at 700 ℃. Because MnO remains as a byproduct at this temperature, we hypothesize that heavy fluorination of DRX materials is attainable in the absence of the redox-active transition metal (Mn). To confirm this hypothesis, we carried out a separate synthesis experiment where a mixture of Li_2TiO_3 and LiF was heated at 800 ℃ for eight hours. This temperature was chosen below the melting point of LiF to avoid any volatility. In **Figure 1d**, the XRD pattern of the resulting synthesis product displays only peaks associated with the DRX phase, with no apparent impurity phases. The positions and intensities of the observed DRX peaks match those of a hypothetical solid solution between Li_2TiO_3 and LiF, assuming Vegard's law. This result parallels our findings from the conventional DRX synthesis procedure and verifies that Ti-based DRX oxyfluorides can be heavily fluorinated if they do not contain Mn. From the perspective of cathode research, however, Mn is needed to enable a high reversible redox capacity over a practical voltage window (e.g., 2.3-4.6 V versus Li/Li^+) [7]. Therefore, we investigated whether MnO can be incorporated into the fluorinated DRX phase using a two-step synthesis procedure: Li_3TiO_3F was first synthesized, then mixed with MnO and held at 800 ℃ for 16 hours. Even after this long hold time, MnO peaks remain clearly visible in the corresponding XRD pattern (**Supplementary Figure S2**). Hence, we conclude that MnO cannot be completely incorporated into the highly fluorinated DRX phase under reasonable temperatures and hold times.

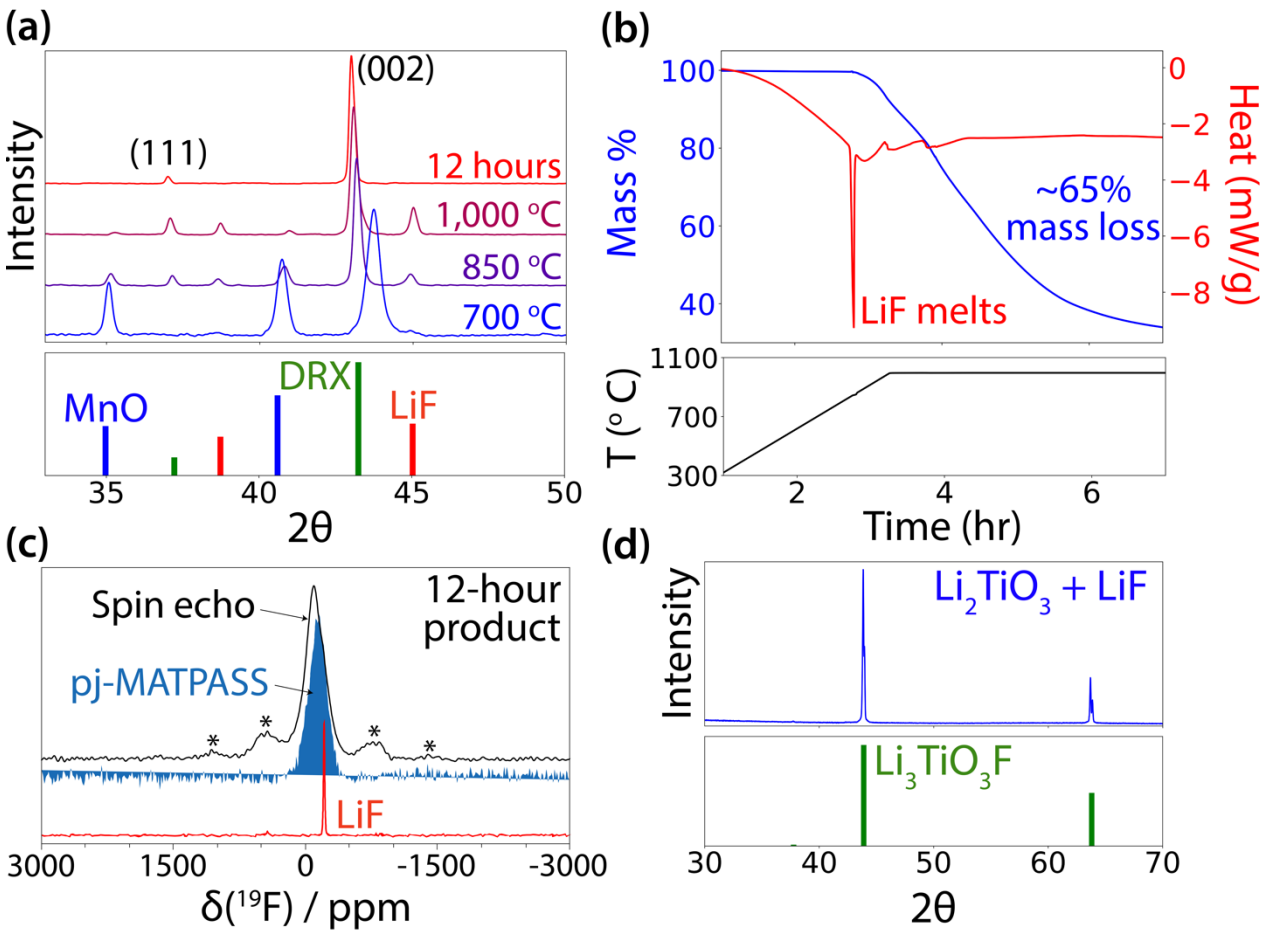

Figure 1. (a) XRD patterns (Cu K_α) from syntheses targeting $Li_{1.2}Mn_{0.4}Ti_{0.4}O_{1.6}F_{0.4}$ using conventional precursors: LiF, MnO, TiO_2, and Li_2CO_3. Each pattern was obtained after heating the precursors to the specified temperature under Ar flow, followed by fast cooling to room temperature. (b) TGA/DSC measurements showing the mass loss and heat curves measured from a sample of LiF annealed at 1000 ℃ as shown in the lower panel. (c) Spin echo (black) and pj-MATPASS [34, 35] (blue shaded area) ^{19}F NMR spectra collected on the 12-hour synthesis product shown in panel (a). Sidebands due to magic angle spinning (MAS) are observed in the spin echo spectrum and denoted with asterisks, while the pj-MATPASS spectrum indicates the distribution of ^{19}F chemical shifts in the sample (spinning sidebands suppressed). A reference ^{19}F spin echo spectrum obtained on pure LiF powder (red) is shown for comparison. (d) XRD pattern measured from the synthesis product of Li_2TiO_3 and LiF, which matches the pattern calculated by Vegard's law (Li_2TiO_3-LiF) for a disordered rocksalt phase, Li_3TiO_3F, shown in the lower panel.

Selection of alternative precursors

Based on the filters described in the Methods, our computational search resulted in 341 precursor sets that are suspected to enhance F solubility. The full list of precursors and their properties are given in **Supplementary Table S1**. To determine which of these sets warrant experimental investigation, we consider the tradeoff between two key metrics: the driving force to form $Li_{1.2}Mn_{0.4}Ti_{0.4}O_{1.6}F_{0.4}$ and the driving force to form LiF, hereafter denoted as $\Delta G_{\text{rxn}}(\text{DRX})$ and $\Delta G_{\text{rxn}}(\text{LiF})$, respectively. An ideal set of precursors should be sufficiently reactive such that DRX formation is favorable, $\Delta G_{\text{rxn}}(\text{DRX}) < 0$, and the magnitude of the associated driving force, $|\Delta G_{\text{rxn}}(\text{DRX})|$, is large. However, the precursors should not be so reactive as to produce LiF as an intermediate phase, which would lower μ_{F} and inhibit fluorination of the DRX phase. To succinctly represent this task, we frame it as a multi-objective optimization problem where the goal is to identify precursor sets occupying the Pareto front [36] of maximal $|\Delta G_{\text{rxn}}(\text{DRX})|$ and minimal $|\Delta G_{\text{rxn}}(\text{LiF})|$, assuming both are negative.

In **Figure 2a**, we present a scatter plot where each point represents a distinct precursor set and the axes show $\Delta G_{\text{rxn}}(\text{DRX})$ versus $\Delta G_{\text{rxn}}(\text{LiF})$ for those sets. The red dashed line represents the Pareto front, which illustrates an optimal tradeoff between these two metrics. Five precursor sets are found to occupy the Pareto front – three of these are listed in **Figure 2b** and two in **Table S1**. Interestingly, all five precursor sets on the Pareto front contain MnF_2, which is a particularly promising fluorinating agent for several reasons. First and foremost, MnF_2 stabilizes F much less than LiF, and is therefore suspected to raise the F solubility limit. This is quantifiable by comparing the lower bound on μ_F where MnF_2 is stable (stable at $\mu_F \geq -4.49$ eV) compared to LiF ($\mu_F \geq -6.36$ eV), as well as other transition metal fluorides (e.g., TiF_3 is stable at $\mu_F \geq -4.92$ eV). Second, MnF_2 places Mn in the proper oxidation state (Mn^{2+}) to synthesize $Li_{1.2}Mn_{0.4}Ti_{0.4}O_{1.6}F_{0.4}$ without requiring any oxidation or reduction. Last, in comparison to TiF_3, MnF_2 has a weaker driving force to form LiF when combined with Li-containing precursors. For example, one may compare the following reactions with Li_2O:

$$MnF_2 + Li_2O \rightarrow MnO + 2\ LiF\ (\Delta G \approx -255\ \text{meV/atom}) \quad (1)$$

$$2\ TiF_3 + 3\ Li_2O \rightarrow Ti_2O_3 + 6\ LiF\ (\Delta G \approx -387\ \text{meV/atom}) \quad (2)$$

Where the reaction energies are normalized per atom of the product phase(s) formed, ensuring a consistent comparison between reactions having different stoichiometries. The moderate reactivity of MnF_2 leads to a good balance between $\Delta G_{\text{rxn}}(\text{DRX})$ and $\Delta G_{\text{rxn}}(\text{LiF})$, which justifies its presence

in all five precursor sets occupying the Pareto front. Of these five sets, one contains elemental Ti, which is difficult to work with owing to its ease of oxidation, while another has a weak driving force to form the targeted phase, with $\Delta G_{\text{rxn}}(\text{DRX}) \approx -4.2$ meV/atom. Accordingly, we exclude these two sets (listed near the top of **Table S1**) from further consideration. The remaining three precursor sets occupying the Pareto front were chosen to be investigated experimentally as they contain readily synthesizable precursors, are straightforward to handle, and have a strong driving force to form $Li_{1.2}Mn_{0.4}Ti_{0.4}O_{1.6}F_{0.4}$. These sets are summarized in **Figure 2b** and detailed in the following three paragraphs.

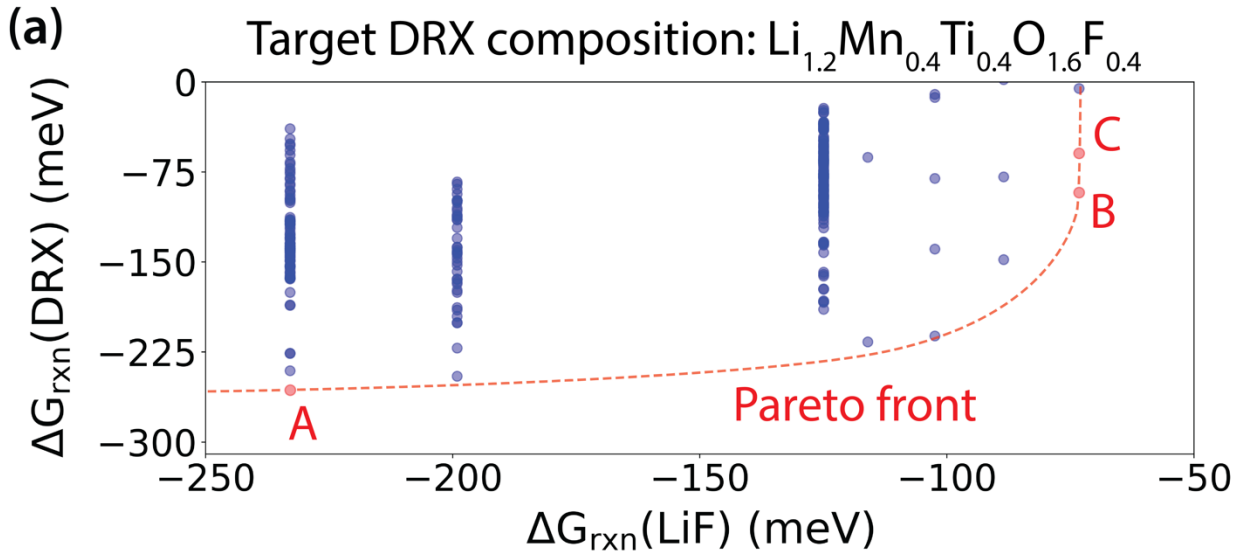

(b) Synthesis routes for experimental investigation:

Precursor sets	ΔG_{rxn}(DRX)	ΔG_{rxn}(LiF)	Label
$Li_6MnO_4 + MnF_2 + 2\,TiO_2$	-256.7 meV	-232.9 meV	A
$2\,LiMnO_2 + 4\,Li_2TiO_3 + MnF_2 + 2\,LiF + Mn$	-91.7 meV	-73.3 meV	B
$2\,LiMnO_2 + 3\,Li_2TiO_3 + MnF_2 + LiF + C$	-57.9 meV	-73.3 meV	C

Figure 2. (a) All suitable precursors sets are plotted in terms of their driving forces to form the targeted DRX phase ($Li_{1.2}Mn_{0.4}Ti_{0.4}O_{1.6}F_{0.4}$) versus the driving force to form LiF. Reaction energies are normalized per atom of product phase (DRX/LiF) formed. (b) Three sets chosen to be investigated experimentally are listed in Table (b) and highlighted red in Panel (a).

Set A: Li_6MnO_4, MnF_2, TiO_2. In this precursor set, MnF_2 is used as the single source of F. Because LiF is absent, there is a large driving force to form the targeted DRX oxyfluoride, with $\Delta G_{\mathrm{rxn}}(\mathrm{DRX}) \approx -256.7$ meV/atom. Another key component of this set is Li_6MnO_4, which has been previously synthesized [37] and is the only stable Mn^{2+}-containing lithium manganese oxide reported in the Materials Project [19]. Because it contains Mn^{2+}, Li_6MnO_4 can be used to synthesize $Li_{1.2}Mn_{0.4}Ti_{0.4}O_{1.6}F_{0.4}$ without requiring any oxidation or reduction. Moreover, Li_6MnO_4 has a less negative formation energy ($E_{\mathrm{F}} \approx -2.06$ eV/atom) than comparative lithium manganese oxides such as $LiMnO_2$ ($E_{\mathrm{F}} \approx -2.17$ eV/atom) and $LiMn_2O_4$ ($E_{\mathrm{F}} \approx -2.08$ eV/atom), where E_{F} is calculated relative to the elemental ground states (Li, Mn, O_2). This also contributes to the large driving force for DRX formation from these precursors; although, the reactivity of Li_6MnO_4 also leads to a moderately high driving force to form LiF through the following reaction:

$$3\ MnF_2 + Li_6MnO_4 \rightarrow 6\ LiF + 4\ MnO \quad (\Delta G_{\mathrm{rxn}} = -232.9\ \mathrm{meV/atom}) \qquad (3)$$

The magnitude of $\Delta G_{\mathrm{rxn}}(\mathrm{LiF})$ is less than that of $\Delta G_{\mathrm{rxn}}(\mathrm{DRX})$, but experimental synthesis with *in situ* characterization presented below will verify which occurs first.

Set B: $LiMnO_2$, Li_2TiO_3, LiF, MnF_2, Mn. There are two F-containing precursors in this set, LiF and MnF_2, which form a eutectic system with a melting point of 600 ℃ [27]. We anticipate that this combination can provide both thermodynamic and kinetic benefits for oxyfluoride synthesis. Because the enthalpy of the mixture can be approximated as an average of LiF and MnF_2 just above its melting point (600 ℃), this mixture has a higher F chemical potential ($\mu_F = -5.73$ eV/atom) than pure LiF and should therefore be more reactive. The molten phase may also facilitate DRX formation by providing a medium for rapid diffusion of precursor atoms [38]. In addition to LiF, both $LiMnO_2$ and Li_2TiO_3 provide sources of Li for DRX synthesis. Because $LiMnO_2$ contains Mn^{3+} as opposed to the Mn^{2+} oxidation state needed for $Li_{1.2}Mn_{0.4}Ti_{0.4}O_{1.6}F_{0.4}$ synthesis, elemental Mn is introduced as a precursor to lower the average oxidation state (1 Mn^0 per 2 Mn^{3+}). In contrast to Li_6MnO_4, as used in the previous precursor set, $LiMnO_2$ is more stable and therefore reduces the driving force to form LiF:

$$MnF_2 + 2\ LiMnO_2 \rightarrow 2\ LiF + Mn_3O_4 \quad (\Delta G_{\mathrm{rxn}} = -73.3\ \mathrm{meV/atom}) \qquad (4)$$

Though, the use of $LiMnO_2$ also leads to a weaker driving force for DRX formation, with $\Delta G_{\mathrm{rxn}}(\mathrm{DRX}) \approx -91.7$ meV/atom. Hence, the two sets described thus far sample two different extremes along the Pareto front, illustrating a tradeoff between $\Delta G_{\mathrm{rxn}}(\mathrm{DRX})$ and $\Delta G_{\mathrm{rxn}}(\mathrm{LiF})$.

Set C: $LiMnO_2$, Li_2TiO_3, LiF, MnF_2, C. This precursor set is similar to set B, except Mn is now replaced with carbon to reduce Mn^{3+} (in $LiMnO_2$) to Mn^{2+} (in $Li_{1.2}Mn_{0.4}Ti_{0.4}O_{1.6}F_{0.4}$) through evolution of CO_2 and/or CO. Precursor stoichiometries were also varied to accommodate the expected oxygen loss, leading to a greater proportion of MnF_2. When using this precursor set, the driving force for DRX formation can be tuned by the choice of synthesis conditions because the free energies of the gaseous CO/CO_2 byproducts are highly dependent on temperature. In contrast, the synthesis conditions have a comparatively negligible effect on the driving force to form LiF since no gaseous species participate in the reaction that forms LiF. Therefore, a high synthesis temperature and low partial pressure of CO/CO_2 (e.g., under flowing Ar) should be used to drive DRX formation. At 800 ℃, for example, $\Delta G_{\mathrm{rxn}}(\mathrm{DRX}) \approx -57.9$ meV/atom. If this reaction is successful, excess carbon may also be included as a means of *in situ* carbon coating, which is sometimes used to enhance the conductivity of electrodes [39].

Synthesis experiments

Set A: Li_6MnO_4, 2 TiO_2, MnF_2

In **Figure 3**, we show XRD patterns measured from the synthesis based on a precursor mixture of Li_6MnO_4, 2 TiO_2, and MnF_2. At 200 ℃, a pristine set of diffraction peaks associated with the precursors is observed, indicating that no reactions have yet occurred. Upon heating the sample to 400 ℃, peaks for both MnF_2 and Li_6MnO_4 have completely disappeared. At the same time, new peaks associated with MnO and LiF have emerged. We therefore deduce that MnF_2 and Li_6MnO_4 reacted to form MnO and LiF between 200-400 ℃ according to Equation (3). After this reaction has taken place, all F in the system is retained by the intermediate LiF phase, which we expect limits F solubility and precludes the formation of $Li_{1.2}Mn_{0.4}Ti_{0.4}O_{1.6}F_{0.4}$. Higher temperatures were explored to confirm this prediction.

A DRX phase is identified at 600 ℃, accompanied by secondary peaks associated with a spinel-type phase. Relative to measurements at 400 ℃, the MnO and TiO_2 peaks are diminished while the LiF peaks remain mostly unchanged. Assuming some residual Li_6MnO_4 remains after the reaction with MnF_2, we suspect that the following side reaction took place:

$$Li_6MnO_4 + 2\ MnO + 9\ TiO_2 \rightarrow 3\ Li_2MnTi_3O_8\ (\Delta G_{\mathrm{rxn}} = -117.8\ \mathrm{meV/atom}) \quad (5)$$

$Li_2MnTi_3O_8$ has been previously reported as a partially inverse spinel structure (space group $P4_332$) with mixed Li/Mn occupation of the tetrahedral 8*a* sites and Li/Mn/Ti occupation of the

octahedral 16*d* sites [40]. Here, the lattice constant of the observed spinel phase (8.41 Å) is close to that of $Li_2MnTi_3O_8$ reported in past work (8.43 Å). However, some peaks expected for $Li_2MnTi_3O_8$ are absent from our XRD pattern (**Figure 3**), which suggests that our observed spinel phase has higher symmetry than in past reports, likely due to increased cation disorder caused by the high temperature (600 ℃) at which the measurement was carried out. Indeed, the observed diffraction peaks closely resemble those of a higher-symmetry spinel phase, $LiMnTiO_4$ (space group $Fd\bar{3}m$) [41], with the exception of a slight change in lattice constant caused by a difference in Mn/Ti content. The spinel phase appears to be short-lived during our synthesis procedure, as very little of it remains at 800 ℃. A majority weight fraction of the mixture at this temperature can be attributed to a DRX phase, in addition to a small amount of MnO. There is no detectable LiF at this temperature, even though its melting point (848 ℃) has not yet been reached. This finding parallels our earlier results from the conventional DRX synthesis – highly fluorinated DRX materials can be made in the absence of Mn.

After reaching the final synthesis temperature of 900 ℃, the amount of detectable MnO is diminished and the DRX peaks shift toward lower 2θ, suggesting incorporation of the large Mn^{2+} ions. However, we caution that these results should be interpreted carefully as the conditions may give rise to LiF volatility. As discussed earlier in the Results section (*Conventional precursors*) and portrayed in **Figure 1**, LiF is extracted from the DRX phase at temperatures near 850 ℃, above which it begins to evaporate under flowing Ar. It is therefore unlikely that the observed DRX phase in **Figure 3** matches the targeted composition, $Li_{1.2}Mn_{0.4}Ti_{0.4}O_{1.6}F_{0.4}$. In addition to the likely evaporation of LiF, a small amount of MnO remains even after the sample is held at 900 ℃ for six hours. In conclusion, our synthesis trial based on Li_6MnO_4, 2 TiO_2, and MnF_2 was not successful because LiF formation occurred at low temperature (200-400 ℃), well before the desired DRX phase could form. This negates the effect of starting with precursors that include a more reactive F source.

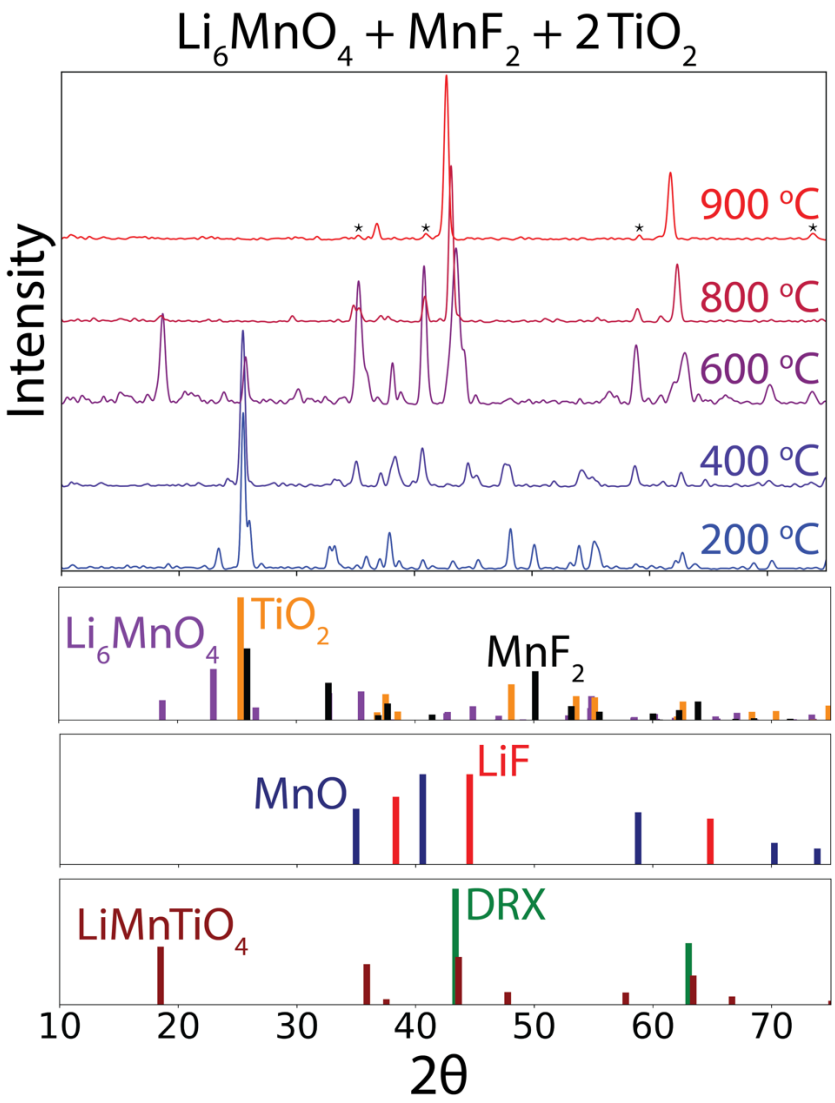

Figure 3. *In situ* XRD (Cu K_α) measured during the synthesis trial of $Li_{1.2}Mn_{0.4}Ti_{0.4}O_{1.6}F_{0.4}$ using precursor set A (MnF_2, Li_6MnO_4, and TiO_2). No ICSD entry is available for Li_6MnO_4, and therefore a DFT-calculated reference (MP #770533) is used. Reference phases include $LiMnTiO_4$ (ICSD #166742), LiF (ICSD #41409), and MnO (ICSD #9864). The final MnO impurity is denoted by asterisks (*) for clarity.

Set B: 2 $LiMnO_2$, 4 Li_2TiO_3, 2 LiF, MnF_2, Mn

In **Figure 4**, XRD patterns are displayed for the products resulting from reactions between 2 $LiMnO_2$, 4 Li_2TiO_3, 2 LiF, MnF_2, and Mn when held at four different temperatures for four hours: 700, 800, 900, and 1000 °C. The pattern measured at 700 °C consists of large diffraction peaks associated with $TiMn_2O_4$, in addition to minor LiF and DRX peaks. Past work indicates that

$TiMn_2O_4$, sometimes written as $Mn(TiMn)O_4$, adopts a spinel structure where the tetrahedral 8*a* sites are predominantly occupied by Mn and the octahedral 16*d* sites are evenly occupied by Mn/Ti [42]. Since no XRD data is available below 700 ℃, some thermodynamic analysis is required to understand which reactions might have led to the formation of $TiMn_2O_4$ as a dominant phase. For this task, we consider all possible reactions between pairs of precursors and identify the one with the largest driving force, $|\Delta G|$, following the principles developed in our previous work to predict synthesis pathways [24, 28]. For the current precursor set, $LiMnO_2$ and MnF_2 comprise the most reactive interface. According to Equation (4), these reactants are expected to produce LiF and Mn_3O_4. Assuming this reaction occurs first, the spinel structure of Mn_3O_4 can provide a template for $TiMn_2O_4$ to form *via* an exchange of Mn/Ti ions between Mn_3O_4 and Li_2TiO_3. This process would also explain why a DRX phase forms at 700 ℃, since Mn/Ti mixing in Li_2TiO_3 leads to increased configurational entropy and favors a disordered rocksalt structure. Because all F ions are trapped within the highly stable LiF phase prior to the formation of the DRX phase, it is unlikely to be highly fluorinated. Hence, avoiding the $LiMnO_2|MnF_2$ reaction (shown to occur < 700 ℃) is critical to oxyfluoride synthesis. The exact temperature and mechanism of this reaction will be discussed in the next Section (precursor set C).

XRD patterns measured from the samples synthesized at 800 and 900 ℃ remain mostly unchanged with respect to 700 ℃, which suggests that the intermediates phases ($TiMn_2O_4$, LiF, and DRX) are slow to react at temperatures below 900 ℃. In contrast, when the sample is heated to 1000 ℃, a new set of peaks associated with $MnTiO_3$ appear. Also at this temperature, the DRX peaks disappear from the pattern, hinting at a transformation from DRX to $MnTiO_3$. The transformation may be caused by Li loss through Li_2O volatility, which is known to occur during DRX syntheses carried out at high temperatures [43] – hence the use of excess Li_2O in conventional precursor mixtures. Some additional Li may also be transferred to $TiMn_2O_4$ between 900 and 1000 ℃. Partial replacement of Mn^{2+} (85 pm) by Li^+ (76 pm) in $TiMn_2O_4$ is evidenced by a small shift in its peak positions toward higher 2θ, indicating a ~0.3% reduction in the lattice constant.

In summary, the precursor mixture of 2 $LiMnO_2$, 4 Li_2TiO_3, 2 LiF, MnF_2, and Mn did not produce the targeted composition, $Li_{1.2}Mn_{0.4}Ti_{0.4}O_{1.6}F_{0.4}$. More generally, our results demonstrate that elemental Mn is not a suitable precursor to synthesize DRX materials, which only ever appeared in minority amounts during the reaction sequence and were completely absent from the

sample made at 1000 °C. Although our synthesis was carried out under an Ar atmosphere with nominally low O_2 content, we suspect that at least some of the metallic Mn precursor was oxidized before it could react with $LiMnO_2$ to reduce the average oxidation state to Mn^{2+}. This is evidenced by the final products being anion rich, consisting predominantly of $TiMn_2O_4$ and $MnTiO_3$.

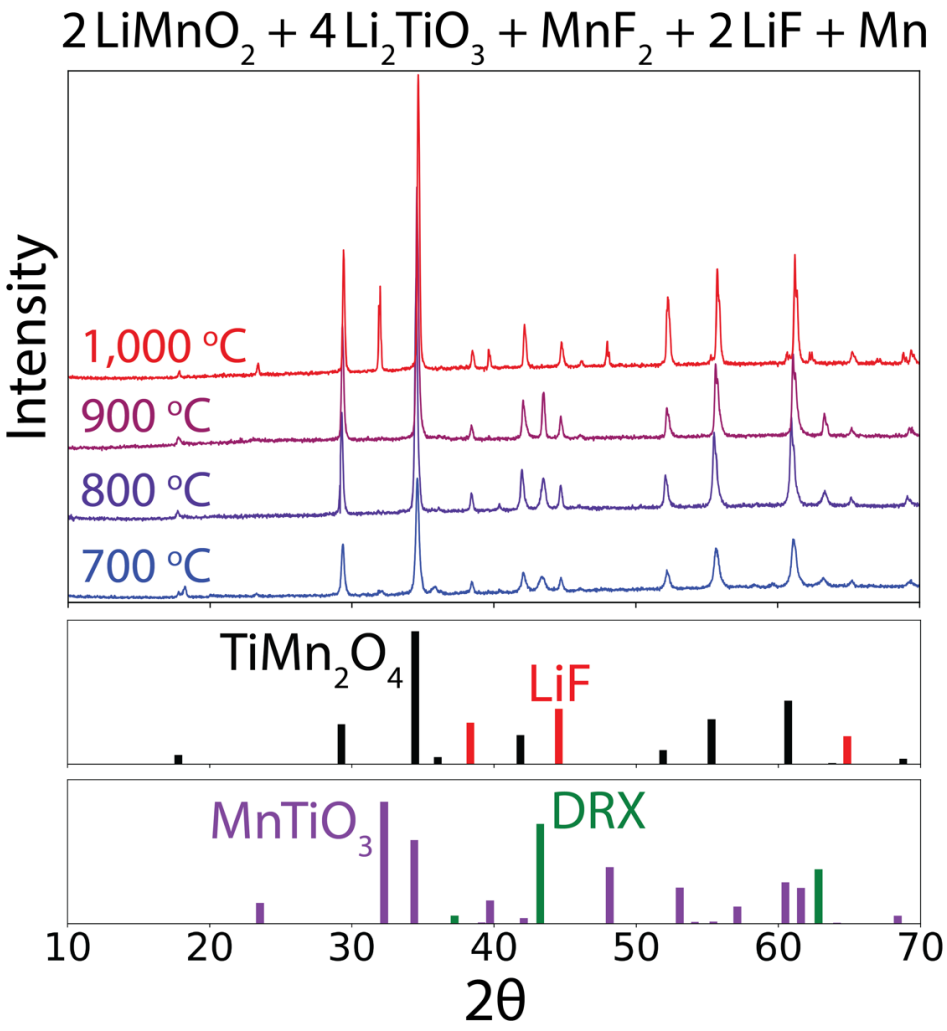

Figure 4. XRD patterns (Cu K_α) measured from samples synthesized at different temperatures using precursor set B (MnF_2, LiF, $LiMnO_2$, Li_2TiO_3, and Mn). Impurity phases include $TiMn_2O_4$ (ICSD #28371), LiF (ICSD #41409), and $MnTiO_3$ (ICSD #60006).

Set C: 2 $LiMnO_2$, 3 Li_2TiO_3, LiF, MnF_2, C

In **Figure 5a**, we present the XRD patterns measured during the synthesis trial based on 2 $LiMnO_2$, 3 Li_2TiO_3, LiF, MnF_2, and C. In contrast to the previous synthesis procedures discussed, synchrotron radiation was used to monitor this route *in situ*, allowing many XRD patterns to be captured with fine temperature resolution. Accordingly, the results are displayed as a heatmap where high (low) diffraction intensities are represented by bright (dark) coloring. We can use the heatmap to pinpoint reaction temperatures and estimate the relative amounts of all intermediate phases. In **Figure 5b**, the corresponding mole fractions are plotted as a function of time, and **Figure 5d** illustrates the relationship between time and temperature by showing the heating profile used during the synthesis procedure.

The first observed reaction initiates at 100 ℃ between MnF_2 and $LiMnO_2$, producing LiF and Mn_3O_4 according to Equation (4). By refining the $LiMnO_2$ peaks, we identify a non-linear contraction in the out-of-plane lattice parameter (*c*) as shown in **Figure 5c**, which coincides with a decrease (increase) in the MnF_2 (LiF) peak intensities. This data suggests that Li extraction from $LiMnO_2$ occurs at temperatures as low as 100 ℃, coupled with the oxidation of Mn^{3+} to Mn^{4+}. The free Li^+ ions facilitate a reaction with MnF_2, forming LiF. The reaction is completed below 500 ℃, above which no MnF_2 is detected. Because this reaction occurs below the eutectic point of LiF-MnF_2 (600 ℃), it precludes the formation of a more reactive fluoride melt, leaving LiF as the single fluorinating agent. The current results parallel our finding from precursor set B, where all MnF_2 was consumed below 700 ℃, and further clarify the $LiMnO_2$|MnF_2 reaction temperature and mechanism. Considering that all F ions are again trapped in LiF, we expect that F solubility will be limited in the resulting DRX product.

The second reaction takes place between Mn_3O_4 and C, with reduction occurring at 700 ℃ to form MnO and CO_2 (and possibly CO) as follows:

$$2\ Mn_3O_4 + C \rightarrow 6\ MnO + CO_2\ (\Delta G_{rxn} = -182\ \text{meV/atom at } 700\ ℃) \quad (6)$$

The reduction of Mn_3O_4 leads to rapid formation of a DRX phase at 700 ℃, in addition to a secondary MnO phase. Simultaneously, there is a large decrease in the amount of Li_2TiO_3 and LiF detected, and therefore the DRX phase formed at 700 ℃ is likely to be highly fluorinated but deficient in Mn. Upon further heating to 932 ℃, increasing incorporation of MnO into the DRX phase is evidenced by a decreased amount of MnO, as well as a shift in the positions of the DRX peaks toward lower 2θ caused by lattice expansion. However, even after the synthesis procedure

is completed and the sample is cooled to room temperature, the MnO byproduct remains apparent and comprises ~5% mole fraction of the DRX/MnO mixture. Although the downward trend in mole fraction of MnO (**Figure 5b**) might suggest that a pure DRX phase can be obtained with longer hold times, we again caution that LiF volatility must be considered at temperatures above 848 °C. Therefore, the observed incorporation of MnO into the DRX phase likely coincides with LiF loss, which would imply that the resulting product is deficient in Li/F and does not match our targeted composition, $Li_{1.2}Mn_{0.4}Ti_{0.4}O_{1.6}F_{0.4}$.

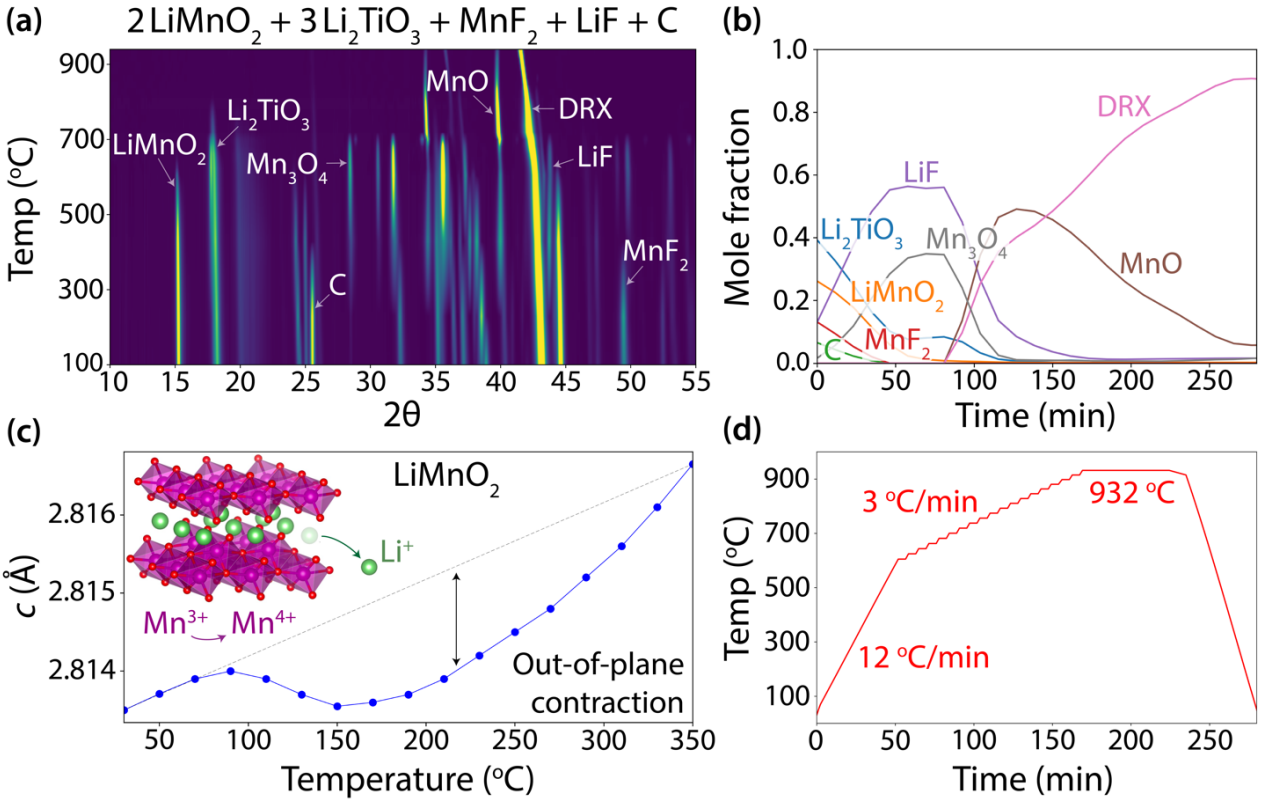

Figure 5. (a) *In situ* synchrotron XRD measurements (converted to Cu K_α) captured during the synthesis trial of $Li_{1.2}Mn_{0.4}Ti_{0.4}O_{1.6}F_{0.4}$ using precursor set C (MnF_2, LiF, $LiMnO_2$, Li_2TiO_3, and C). Only the heating step is shown. (b) Refined mole fractions of all crystalline phases are plotted as a function of time, neglecting any molten or amorphous phases. (c) The out-of-plane $LiMnO_2$ lattice constant is refined as a function of temperature, showing a non-linear contraction associated with Li^+ extraction. (d) The heating profile used during the synthesis procedure.

In precursor set C, the limited F solubility can be traced back to the reaction between $LiMnO_2$ and MnF_2, which forms LiF and lowers the F chemical potential, μ_F. As discussed earlier, this reaction begins at a low temperature (100 ℃) because Li^+ is easily extracted from the layered $LiMnO_2$ structure, coupled with oxidation of Mn^{3+} to Mn^{4+}. Considering this problem, we aim to avoid topotactic Li removal by replacing $LiMn^{3+}O_2$ with $Li_2Mn^{4+}_{0.33}Ti_{0.66}O_3$ as a novel precursor for DRX synthesis. Extracting Li^+ ions from this compound would require oxidation beyond Mn^{4+}, which is unlikely to occur given its high ionization energy. In other words, $Li_2Mn^{4+}_{0.33}Ti_{0.66}O_3$ is designed to "lock in" the Li^+ ions and prevent LiF formation. If successful, this would allow MnF_2 to be retained until high temperatures where the DRX can form, thereby keeping μ_F high such that F solubility is improved in the final product.

We synthesized $Li_2Mn_{0.33}Ti_{0.66}O_3$ by heating a mixture of Li_2MnO_3 and Li_2TiO_3 to 900 ℃ for eight hours under flowing Ar. In **Figure 6a**, the XRD pattern of the resulting sample is shown. The observed lattice constants (5.001, 8.649, and 5.090 Å) closely match those predicted by Vegard's law (5.003, 8.644, and 5.096 Å) between Li_2MnO_3 and Li_2TiO_3, assuming a layered monoclinic structure for both phases. Furthermore, there are no impurity peaks in the pattern, indicating a successful synthesis. Next, we mixed $Li_2Mn_{0.33}Ti_{0.66}O_3$ with MnF_2 and C, which serve as fluorinating and reducing agents, respectively. The mixture was held at 800 ℃ for four hours to synthesize $Li_{1.2}Mn_{0.4}Ti_{0.4}O_{1.6}F_{0.4}$. The XRD pattern of the resulting synthesis product is displayed in **Figure 6b**. A DRX phase does indeed comprise a majority weight fraction of the mixture; however, three impurity phases also appear in addition to leftover carbon: $TiMn_2O_4$, LiF, and MnO. These results point to the following side reaction:

$$6\ MnF_2 + 2\ Li_2Mn_{0.33}Ti_{0.66}O_3 + C \rightarrow 4\ TiMn_2O_4 + 12\ LiF + CO_2 \quad (7)$$

Hence, LiF formation was not prevented by "locking in" Li^+ ions with a Mn^{4+}-based precursor. Even when a lower temperature of 400 ℃ was used, all MnF_2 was consumed to form LiF, further supporting the strong driving force and fast kinetics of the reaction.

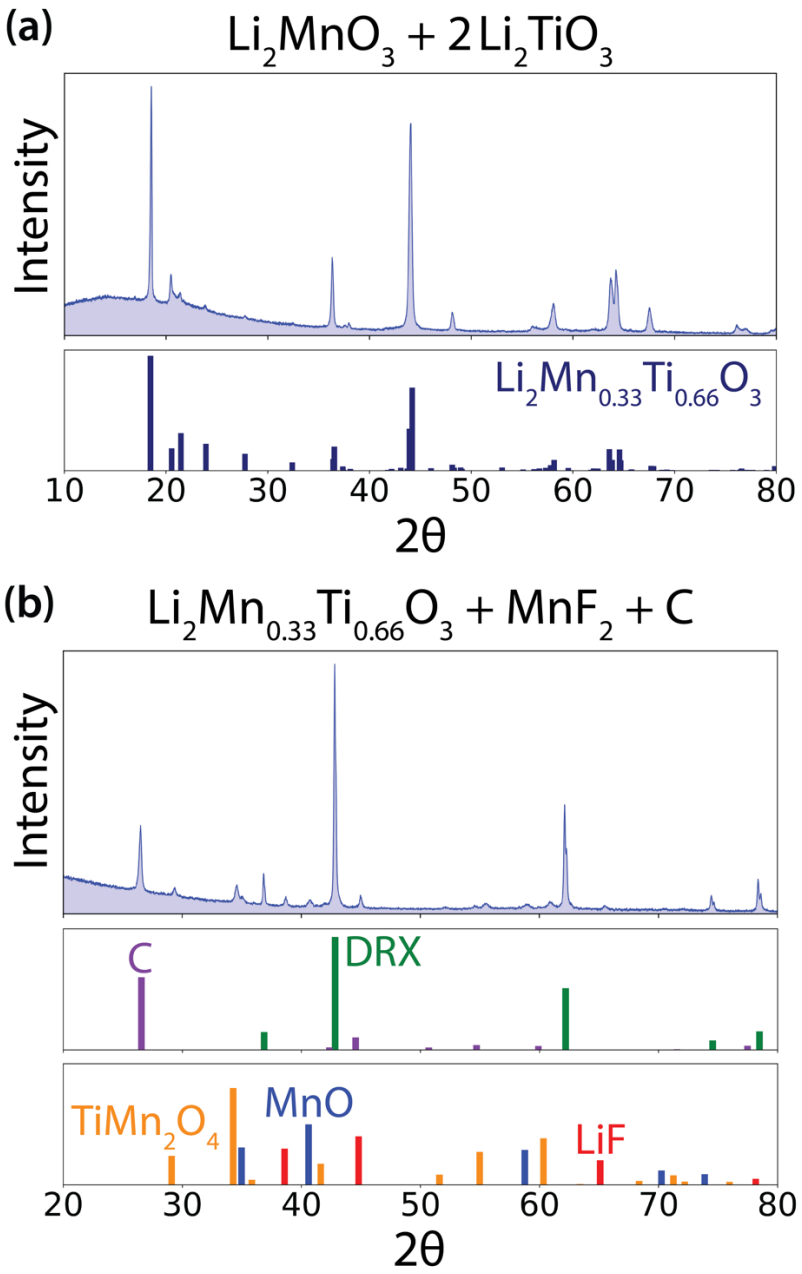

Figure 6. (a) XRD pattern (Cu K_α) measured from the sample with a nominal composition of $Li_{1.33}Mn_{0.22}Ti_{0.44}O_2$, which matches well with the corresponding diffraction pattern calculated for a solid solution between Li_2MnO_3 and Li_2TiO_3. (b) XRD pattern (Cu K_α) measured from the synthesis product using $Li_{1.33}Mn_{0.22}Ti_{0.44}O_2$, MnF_2, and C precursors. The impurity phases include MnO (ICSD #9864), LiF (ICSD #41409), $TiMn_2O_4$ (ICSD #28371), and C (ICSD #76767).

Table 1: A summary of the reaction data obtained from all precursor sets tested in this work. The observed phases listed at each temperature include leftover precursors, intermediate phases, and final products. These are listed in order of decreasing weight fraction. All phases labeled "DRX" adopt a disordered rocksalt structure but may have different compositions.

Precursors	Temp. (°C)	Observed phases
LiF, MnO, TiO_2, Li_2CO_3	700	DRX, MnO
	850	DRX, MnO, LiF
	1000	DRX, LiF
LiF, Li_2TiO_3	800	Li_3TiO_3F
Li_6MnO_4, MnF_2, TiO_2	400	MnO, TiO_2, LiF, Li_6MnO_4
	600	DRX, $Li_2MnTi_3O_8$, MnO, TiO_2, LiF
	800	DRX, MnO, $Li_2MnTi_3O_8$
	900	DRX, MnO
$LiMnO_2$, Li_2TiO_3, MnF_2, LiF, Mn	700	$TiMn_2O_4$, LiF, DRX
	1000	$TiMn_2O_4$, $TiMnO_3$, DRX
$LiMnO_2$, Li_2TiO_3, MnF_2, LiF, C	100	$LiMnO_2$, Li_2TiO_3, Mn_3O_4, C, LiF
	700	DRX, MnO
$Li_2Mn_{0.33}Ti_{0.66}O_3$, MnF_2, C	800	DRX, $TiMn_2O_4$, MnO, LiF

Discussion

In **Table 1**, we summarize the reaction pathways characterized in this work. Our characterization of DRX synthesis from conventional precursors (Li_2CO_3, TiO_2, MnO, and LiF) reveals several key reaction steps that dictate the composition of the final product. A highly fluorinated, but Mn-deficient, DRX phase forms at 700 ℃, leaving MnO as a secondary phase that does not react until higher temperature. The existence of such a fluorinated DRX phase was verified through a separate experiment where Li_3TiO_3F was successfully synthesized from Li_2TiO_3 and LiF. These results confirm previous theoretical speculation that high Li content and the use of d^0 elements (e.g., Ti) enhance F solubility in DRX materials, but incorporation of later transition metals (e.g., Mn) reduces F solubility due to the relatively weak bonds formed between Mn-F compared to Li-F [4,

14, 44]. Although MnO can react with the highly fluorinated, Mn-deficient DRX phase at temperatures above 850 ℃, it also leads to the removal of LiF from the DRX phase, followed by evaporation of LiF from the sample. The volatility of LiF was confirmed by our TGA/DSC studies, which show that evaporation begins at 848 ℃ and becomes more rapid when held at higher temperatures, with only 35% of the starting mass remaining after five hours at 1000 ℃. Because much of the LiF precursor evaporates during synthesis, the resulting DRX phase has lower F content than expected based on the precursor stoichiometry. This is further evidenced by a weak ^{19}F signal from our NMR measurements on the final synthesis product.

As demonstrated by our computational search for new precursor sets targeting $Li_{1.2}Mn_{0.4}Ti_{0.4}O_{1.6}F_{0.4}$, there exist many possible synthesis routes that start with high μ_F by using a reactive F source such as MnF_2. In principle, these routes should lead to enhanced F solubility if the precursors directly contribute to DRX formation. However, our experiments show that this is not the case; DRX formation is always preceded by a series of intermediate phases resulting from reactions between precursor pairs. Importantly, the first reaction to occur in each synthesis route involves the formation of LiF, which negates the effects of starting from a more reactive F source and limits F solubility in any Mn-containing DRX phase formed at higher temperature.

The first reaction to take place in each synthesis path also dictates the temperature at which DRX formation proceeds. When Li_6MnO_4 is included in the precursor set, it reacts with MnF_2 to form LiF and MnO between 200-400 ℃. Because MnO places Mn in the same oxidation state as the targeted phase (Mn^{2+}), no oxidation or reduction is required in later reactions. This enables the formation of a DRX phase at relatively low temperature (600 ℃), though it competes with a secondary spinel phase ($Li_2MnTi_3O_8$) that requires further heating to consume. In contrast, when $LiMnO_2$ is included in the precursor set, it reacts with MnF_2 between 100-400 ℃ to form LiF and Mn_3O_4. Since Mn_3O_4 has a mixed oxidation state (Mn^{2+}/Mn^{3+}), it must be reduced before it can contribute to DRX formation, raising the required synthesis temperature. When a carbon precursor is used as a reducing agent, it successfully reduces Mn_3O_4 at 700 ℃ and a DRX phase is formed shortly thereafter with only a minor MnO impurity phase. If Mn is alternatively used as a reducing agent, it fails to react with Mn_3O_4 and reduce the average Mn oxidation state to Mn^{2+}. Instead, an exchange reaction between Mn_3O_4 and Li_2TiO_3 replaces Mn^{3+} with Ti^{4+} to form a dominant spinel phase, $TiMn_2O_4$, in addition to a secondary DRX phase. These findings suggest that the competition between DRX and spinel phases can be controlled *via* the choice of reducing agent

and synthesis temperature – stronger reducing agents (such as carbon) and higher temperatures favor DRX formation (1:1 cation-anion ratio), whereas weaker reducing agents and lower temperatures favor spinel formation (anion-excess).

Although none of our proposed synthesis routes were successful in forming the targeted composition, $Li_{1.2}Mn_{0.4}Ti_{0.4}O_{1.6}F_{0.4}$, the results provide valuable insight into the factors that control DRX formation and inhibit their fluorination. Indeed, the importance of "dark" reaction data (i.e., failed syntheses) has been detailed in previous work [45], although negative results are rarely reported in the literature. Here, we demonstrate the utility of dark reaction data by using our results to identify three key principles governing F solubility in DRX oxyfluorides. These are illustrated in **Figure 7** and discussed in the following three paragraphs.

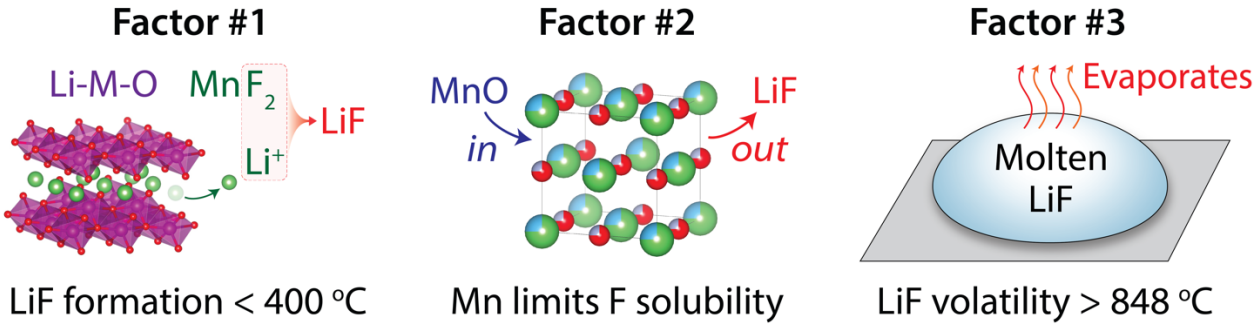

Figure 7. A summary of the three major factors identified in this work that limit F solubility in DRX oxyfluoride materials synthesized by a solid-state approach.

Factor #1: Avoiding LiF is key to maintaining a high F chemical potential (μ_F) and enhancing F solubility. Although MnF_2 was identified as a promising fluorinating agent, we find that it inevitably reacts with any Li-containing precursor ($\leq$ 400 °C) to form LiF as an intermediate phase before the targeted DRX phase can form ($\geq$ 600 °C), thereby limiting its F solubility. Based on our DFT-calculated reaction energies (**Figure 2**), each precursor set was designed to have a stronger thermodynamic driving force to form $Li_{1.2}Mn_{0.4}Ti_{0.4}O_{1.6}F_{0.4}$ than to form LiF – i.e., $|\Delta G_{rxn}(\text{DRX})| > |\Delta G_{rxn}(\text{LiF})|$. It may therefore seem counterintuitive that LiF formation always precedes DRX formation. On the contrary, these findings support previous theories regarding the mechanism of solid-state reactions, which propose that intermediate phases initially nucleate at the interface between the pair of precursors with the highest reactivity (largest ΔG), regardless of the

overall precursor stoichiometry [24, 28]. Reactions at the interfaces can occur *via* short-range diffusion of species from the neighboring precursors, whereas reactions involving the entire precursor mixture would otherwise require diffusion of species over much larger length scales. Consequently, it is kinetically favorable to minimize the free energy locally (at the interfaces between precursors) as opposed to minimizing the free energy globally (for the entire mixture). With respect to the DRX oxyfluoride syntheses studied here, the most reactive precursor pair in each set always consists of MnF_2 and a Li-containing phase, as described by Equations (3) and (4). Hence, although DRX formation is thermodynamically favored based on the entire set of precursors, the local reaction to form LiF at the MnF_2|Li-M-O interface always happens first and dictates the remainder of the reaction pathway.

Factor #2: Our synthesis data shows that highly fluorinated DRX materials can be made in the absence of Mn, confirming our theoretical predictions from past work [14]. Here, Li_3TiO_3F was successfully synthesized without any impurity phases. Obtaining $Li_{1.2}Mn_{0.4}Ti_{0.4}O_{1.6}F_{0.4}$ from Li_3TiO_3F requires a reaction with MnO, yet this reaction is slow to occur even at 1000 ℃, and MnO incorporation into the DRX phase is found to coincide with LiF extraction from it. Based on these findings, we identify Mn as the primary element limiting F solubility in Mn/Ti-based DRX oxyfluorides. To rationalize this conclusion, it is important to understand that the limiting effects of Mn are two-fold. First, previous work has demonstrated that Mn-F bonds are much higher in energy (less favorable) than Li-F bonds [14]. Short-range order in the DRX lattice accommodates Li-rich (Mn-poor) environments surrounding F anions to maximize the number of low-energy Li-F bonds [44]. However, the maximum number of possible Li-rich environments decreases with an increasing Mn content, enforcing reduced (increased) Li-F (Mn-F) coordination. Second, because Mn^{2+} is low-valent relative to Ti^{4+}, any DRX composition with a high Mn^{2+} content is required by charge balance to also have a low Li^+ content. For example, Li_3TiO_3F can be made with a remarkably high F content of 25% owing to its 3:1 Li:TM ratio. In contrast, making a purely Mn^{2+}-based DRX with the same F content (25%) would require a composition of $LiMn_3O_3F$ (1:3 Li:TM ratio). This significantly reduces the number of Li-F bonds, instead replacing them with high-energy Mn-F bonds. The detrimental effect of Mn on F solubility is an unfortunate result in terms of DRX cathodes, given that high Mn content is required to enable a large and reversible redox capacity based on the Mn^{2+}/Mn^{4+} couple. Otherwise, a highly fluorinated composition such as Li_3TiO_3F may only derive capacity from oxygen redox.

Factor #3: For the synthesis of solid solutions, higher temperature is generally expected to increase solubility as it enhances the contributions of configurational entropy to the free energy of the solid solution. One might therefore anticipate that higher F solubility can be achieved in DRX materials by increasing their synthesis temperature. However, we have demonstrated that DRX syntheses carried out at high temperatures (> 848 ℃) are plagued by LiF volatility, which reduces the amount of F incorporated into the final product. Our TGA/DSC data (**Figure 1b**) indicates that LiF loss proceeds directly after it melts at 848 ℃, and continues to evaporate when held above this temperature. Interestingly, LiF volatility appears to be a problem even when the Li/F species are initially incorporated into a highly fluorinated (but Mn deficient) DRX phase such as Li_3TiO_3F. As shown in **Figure 1a**, LiF is extracted from the DRX phase above 850 ℃ and disappears from the XRD pattern when held 1000 ℃ for 12 hours. The evaporation of LiF well below its boiling point of 1,680 ℃ is surprising at first glance, especially considering its low vapor pressure of ~0.1 Torr at 1000 ℃ [46]. However, because the sample is placed under flowing Ar to avoid oxidation of Mn during DRX synthesis, the partial pressure of any gaseous species from the sample is kept low, facilitating LiF evaporation.

Considering the volatility of LiF, we stress that characterization of synthesis products by XRD alone can be misleading when dealing with DRX oxyfluorides made under gaseous flow. The use of high temperatures and long hold times contributes to LiF loss, and therefore the XRD pattern measured from the resulting sample will not contain any diffraction peaks associated with LiF. This does not necessarily prove incorporation of F into the DRX phase, as one might expect. Instead, it may indicate that LiF has evaporated from the sample. Furthermore, we caution that an observed change in the electrochemical properties of a DRX material with respect to an increase in its nominal F content is still insufficient evidence to prove enhanced fluorination. The expected increase in nominal F content can be traced back to a greater LiF precursor stoichiometry. If significant LiF has evaporated from the sample, then the resulting DRX phase will be deficient in Li/F and excess in Mn. In turn, the electrochemical properties will be modified – not due to fluorination, but from higher Mn content.

In conclusion, to be confident in the composition of DRX oxyfluorides synthesized under gaseous flow, we suggest that short annealing times (< 1 hour) or low temperatures (< 848 ℃) should be used. Otherwise, additional characterization techniques are needed to supplement XRD and confirm bulk fluorination of the product. Most notably, TGA/DSC measurements can be used

to confirm LiF mass loss or the absence thereof, and ^{19}F solid-state NMR can provide information on the relative fraction of all F-containing phases in a sample, irrespective of their crystallinity.

Conclusion

We have tested and analyzed several different synthesis pathways targeting DRX oxyfluorides to identify the main factors that limit their F solubility. Despite starting from a more reactive F source, LiF consistently forms *via* intermediate reactions between MnF_2 and the Li-containing precursor, which lowers the F chemical potential and inhibits fluorination of the targeted phase. DRX materials with significantly increased F content (~25%) can be made if they do not contain Mn; however, this limits their usefulness as cathode materials since Mn provides the main redox capability. Higher temperatures enable increased Mn uptake, but this comes at the cost of LiF volatility, resulting in a DRX phase with low F content. To synthesize DRX materials with both high Mn and F content, it is necessary to explore alternative techniques for metastable materials synthesis where kinetic factors become dominant in the reaction mechanism, thereby avoiding the thermodynamic ground state (LiF) that we show substantially limits F solubility in the DRX.

Our findings demonstrate how failed experiments can still be useful to better understand materials synthesis, which often remains a "black box" process that must be optimized through trial-and-error. Several techniques enabling predictive synthesis have recently emerged [47-49], yet none are universally applicable, and more tests are needed to identify their limitations. The theoretical methods used in this work rely on thermodynamics for the design of optimal precursors, yet they fail to capture more subtle effects related to kinetic factors. To improve upon the current approaches to synthesis design, new experimental data is needed. Although negative results are rarely reported in the literature, those reported here provide key insight into the challenges of fluorination. As such, we hope our work sets a precedent for increased publication of failed synthesis data with concurrent interpretation of the results. This would not only contribute to an improved understanding of materials synthesis, but also aid in the development of statistical models for synthesis outcome prediction.

Experimental details

Materials synthesis

A conventional solid-state synthesis procedure was carried out using common precursors from previous work: LiF, MnO, TiO_2, and Li_2CO_3 [7, 8, 50]. Stoichiometric amounts of these precursors, plus 10% excess weight of Li_2CO_3 to compensate for possible Li loss, were mixed in ethanol with five 10 mm and ten 2 mm stainless balls in a 50 mL stainless steel jar using a Retsch PM200 planetary ball mill at 300 rpm for 12 hours. The resulting slurry was dried to form a powder, which was then pressed into a pellet using a 6 mm stainless steel die before heat treatment under an atmosphere of flowing Ar. Three synthesis temperatures were tested (700, 850, and 1000 ℃), each with a one-hour hold time. A longer hold time of 12 hours was also tested at 1000 ℃. After heating, the samples were cooled to room temperature under Ar flow. The final products were manually ground in an Ar-filled glove box for subsequent characterization by XRD and NMR as described in the Characterization section.

Set A: Li_6MnO_4, MnF_2, TiO_2. Because Li_6MnO_4 is not commercially available, we first synthesized it using a procedure outlined in previous work [37]. Stoichiometric amounts of anhydrous Li_2O and MnO were mixed in a high-energy SPEX mill (SPEX SamplePrep 8000M) for two hours. Stainless steel milling media were used in a 10:1 ratio of media to powder. The milled powder was recovered in an Ar-filled glovebox and pressed into pellets using a 13 mm stainless steel die. The pellet was annealed at 950 ℃ for 12 hours under a flowing mixture of 96% Ar and 4% H_2 in a tube furnace. The product was ground manually and its purity was verified by XRD (**Supplementary Figure S2**), which showed good agreement with past results [37]. The DRX oxyfluoride synthesis was then carried out by mixing stoichiometric amounts of Li_6MnO_4, MnF_2, and TiO_2 with a mortar and pestle for 30 minutes in an Ar-filled glovebox. The resulting powder was recovered and used for temperature dependent XRD measurements detailed in the Characterization section.

Set B: $LiMnO_2$, Li_2TiO_3, LiF, MnF_2, Mn. Stoichiometric amounts of these precursors were sufficiently mixed for 12 hours. The mixture was loaded into an alumina crucible and sealed inside a quartz tube under an Ar atmosphere. The vessel was then heated to the designated synthesis temperature with a ramp rate of 10 ℃/minute and annealed at that temperature for four hours, followed by a natural cool to room temperature. Four synthesis temperatures were tested

(700, 800, 900, and 1000 ℃). The final products were harvested by cutting the sealed tube, stored inside an Ar-filled glovebox, and ground into a powder that was then characterized by XRD.

Set C: $LiMnO_2$, Li_2TiO_3, LiF, MnF_2, C. Stoichiometric amounts of these precursors, plus 5% excess weight of carbon, were mixed in ethanol with five 10 mm and ten 2 mm stainless balls in a 50 mL stainless steel jar using a Retsch PM200 planetary ball mill at 300 rpm for 12 hours. The slurry was then dried and pelletized before being sent to a beamline facility for *in situ* characterization by synchrotron XRD. A synthesis temperature of 932 ℃ was used under an atmosphere of flowing N_2. A detailed description of the heating profile is given in the Characterization section.

Two additional synthesis procedures targeting $Li_{1.2}Mn_{0.4}Ti_{0.4}O_{1.6}F_{0.4}$ were carried out with the following precursor sets: (1) $Li_2Mn_{0.33}Ti_{0.66}O_3$, MnF_2, and C; (2) Li_3TiO_3F and MnO. For set (1), $Li_2Mn_{0.33}Ti_{0.66}O_3$ was first synthesized by mixing stoichiometric amounts of Li_2MnO_3 and Li_2TiO_3 *via* wet ball milling, following the same procedure as described for precursor set C. The mixture was heated at 900 ℃ for eight hours under an atmosphere of flowing Ar, followed by a natural cool to room temperature. The product was manually ground in an Ar-filled glove box and characterized by XRD. Next, stoichiometric amounts of $Li_2Mn_{0.33}Ti_{0.66}O_3$, MnF_2, and carbon were mixed *via* wet ball milling and heated at 800 ℃ for four hours under flowing Ar. The product was naturally cooled, ground in an Ar-filled glovebox, and characterized by XRD. For set (2), Li_3TiO_3F was first synthesized by mixing Li_2TiO_3 and LiF *via* wet ball milling and subsequently dried to form a powder, which was heated at 800 ℃ for eight hours in air. The product was naturally cooled, extracted, and ground into a powder. To synthesize $Li_{1.2}Mn_{0.4}Ti_{0.4}O_{1.6}F_{0.4}$, stoichiometric amounts of Li_3TiO_3F and MnO were mixed following the same procedure as Li_3TiO_3F, followed by heating at 800 ℃ under an atmosphere of flowing Ar for 16 hours. The product was naturally cooled, extracted in an Ar-filled glovebox, and characterized by XRD.

Characterization

Samples made from LiF, MnO, TiO_2, and Li_2CO_3 were characterized by *ex situ* XRD using a Rigaku MiniFlex 600 diffractometer with Cu K_α radiation ($\lambda = 1.54178$ Å). The volatility of LiF during the synthesis procedure was studied by heating a pure sample of LiF powder at a rate of 5 ℃/minute to 1000 ℃ with a hold time of five hours while *in situ* TGA/DSC measurements were carried out using a Q600 SDT instrument. Solid-state NMR was also performed on the synthesis

products of LiF, MnO, TiO_2, and Li_2CO_3 heated at 1000 ℃ for 12 hours to check whether any LiF was present in the sample. These measurements were conducted using a wide bore Bruker BioSpin spectrometer ($B_0 = 2.35$ T, 100 MHz for ^{1}H) equipped with a DMX 500 MHz console and a custom-made 1.3 mm X-broadband magic angle spinning (MAS) probe tuned to ^{19}F (94.1 MHz). Samples were packed in zirconia rotors in an Ar-filled glovebox and spun at $\upsilon_R = 60$ kHz using dry nitrogen. ^{19}F chemical shifts was externally referenced against pure LiF powder, with $\delta_{\mathrm{iso}}(^{19}\mathrm{F}) = -204$ ppm. ^{19}F NMR spectra was obtained using a rotor-synchronized spin echo sequence ($90° - \tau_R - 180° - \tau_R$) with a 90° RF pulse of 0.35 µs, and data was averaged over 7168 transients with a recycle delay of 50 ms between scans. Additionally, isotropic ^{19}F NMR spectra was recorded using the projected magic angle turning phase-adjusted sideband separation (pj-MATPASS) pulse sequence [34, 35], which effectively removes sidebands due to MAS. This experiment used the same 90° RF pulse as the ^{19}F spin echo. Result was averaged over 2000 scans with a recycle delay of 50 ms. Solid-state NMR data were processed using the Bruker TopSpin 3.6.0 software and spectra were fitted using the DMfit software [51].

Ex situ XRD patterns of the synthesis products from sets A-C were measured using a Scintag XDS 2000, Bruker D2-Phaser, and Rigaku MiniFlex 600 diffractometer, respectively, each with Cu K_α radiation. For precursors set A, *in situ* XRD measurements were also performed by using a Malvern PANalytical X'Pert Pro MPD diffractometer (45 kV, 40 mA) equipped with an Anton Paar XRK-900 reaction chamber operated in $2q$-q mode. During these measurements, Ar gas was used to purge the reaction chamber and avoid unwanted oxidation of the sample. Cu K_α radiation was used to collect XRD data at temperature intervals of 100 ℃, ranging from 100-900 ℃. A heating rate of 10 ℃/minute was used between each hold temperature, which was equilibrated for one minute prior to data collection.

For precursor set C, experiments were conducted with Beamline 28-ID-2 of the National Synchrotron Light Source II (NSLS-II) at Brookhaven National Laboratory. An X-ray wavelength of 0.1846 Å was used. The powder samples were pressed into pellets of 0.5 mm in thickness and 7mm in diameter before loading into a Linkam TS1500 furnace A two-dimensional X-ray detector (Perkin-Elmer XRD 1621), placed at 1493 mm from the sample, was used to collect XRD patterns during the heating procedure. A heating rate of 12 ℃/minute was used for temperatures up to 600 ℃, followed by a heating rate of 3 ℃/minute up to 932 ℃. For calibration based on thermal

expansion, XRD patterns from a CeO_2 standard powder (NIST SRM 674b) were measured at the same conditions as the DRX samples.

Supporting Information

Visualization of chemical potentials for different fluoride precursors, supplementary X-ray diffraction patterns, and a list of all precursor sets identified with computational screening.

Acknowledgements

This work was supported by the Assistant Secretary for Energy Efficiency and Renewable Energy, Vehicle Technologies Office, under the Applied Battery Materials Program, of the US Department of Energy (DOE) under contract no. DE-AC02-05CH11231 and by Umicore Specialty Oxides and Chemicals. We also acknowledge support from the National Science Foundation Graduate Research Fellowship under grant #1752814. The NMR results reported here made use of shared facilities of the UCSB MRSEC (NSF DMR #1720256), a member of the Materials Research Facilities Network (www.mfn.org). X-ray data measurement and part of XRD data analysis were conducted at the Center for Nanophase Materials Sciences (CNMS), which is a DOE Office of Science User Facility.

References

1. Clément, R.J., Z. Lun, and G. Ceder, *Cation-disordered rocksalt transition metal oxides and oxyfluorides for high energy lithium-ion cathodes.* Energy & Environmental Science, 2020. **13**: p. 345-373.
2. Lee, J., et al., *Unlocking the Potential of Cation-Disordered Oxides for Rechargeable Lithium Batteries.* Science, 2014. **343**: p. 519-522.
3. Lee, J., et al., *Determining the Criticality of Li-Excess for Disordered-Rocksalt Li-Ion Battery Cathodes.* Advanced Energy Materials, 2021: p. 2100204.
4. Lun, Z., et al., *Design Principles for High-Capacity Mn-Based Cation-Disordered Rocksalt Cathodes.* Chem, 2020. **6**: p. 153-168.
5. Yang, M., et al., *Cation-Disordered Lithium-Excess Li–Fe–Ti Oxide Cathode Materials for Enhanced Li-Ion Storage.* ACS Applied Materials & Interfaces, 2019. **11**(47): p. 44144044152.
6. Li, H., et al., *Toward high-energy Mn-based disordered-rocksalt Li-ion cathodes.* Joule, 2022. **6**: p. 53-91.
7. Lee, J., et al., *Reversible Mn2+/Mn4+ double redox in lithium-excess cathode materials.* Nature, 2018. **556**: p. 185-190.
8. Chen, D., et al., *Understanding cation-disordered rocksalt oxyfluoride cathodes.* Journal of Materials Chemistry A, 2021. **9**: p. 7826.

9. Chen, R., et al., *Li+ intercalation in isostructural Li2VO3 and Li2VO2F with O2− and mixed O2−/F− anions.* Physical Chemistry Chemical Physics, 2015. **17**: p. 17288.
10. Takeda, N., et al., *Reversible Li storage for nanosize cation/anion-disordered rocksalt-type oxyfluorides: LiMoO2 – x LiF (0 ≤ x ≤ 2) binary system.* Journal of Power Sources, 2017. **367**: p. 122-129.
11. Li, L., et al., *Fluorination-Enhanced Surface Stability of Cation Disordered Rocksalt Cathodes for Li-Ion Batteries.* Advanced Functional Materials, 2021. **31**: p. 2101888.
12. Yue, Y., et al., *Tailoring the Redox Reactions for High-Capacity Cycling of Cation-Disordered Rocksalt Cathodes.* Advanced Functional Materials, 2021. **31**: p. 2008696.
13. Lun, Z., et al., *Improved Cycling Performance of Li-Excess Cation-Disordered Cathode Materials upon Fluorine Substitution.* Advanced Energy Materials, 2018. **9**: p. 1802959.
14. Ouyang, B., et al., *Effect of Fluorination on Lithium Transport and Short Range Order in Disordered-Rocksalt-Type Lithium-Ion Battery Cathodes.* Advanced Energy Materials, 2020. **10**: p. 1903240.
15. Chen, R., et al., *Disordered Lithium-Rich Oxyfluoride as a Stable Host for Enhanced Li + Intercalation Storage.* Advanced Energy Materials, 2015. **5**: p. 1401814.
16. Schlem, R., et al., *Energy Storage Materials for Solid-State Batteries: Design by Mechanochemistry.* Advanced Energy Materials, 2021. **11**: p. 2101022.
17. Shi, T., et al., *High Active Material Loading in All-Solid-State Battery Electrode via Particle Size Optimization.* Advanced Energy Materials, 2019: p. 1902881.
18. Ahn, J., D. Chen, and G. Chen, *A Fluorination Method for Improving Cation-Disordered Rocksalt Cathode Performance.* Advanced Energy Materials, 2020. **10**: p. 2001671.
19. Jain, A., et al., *The Materials Project: A materials genome approach to accelerating materials innovation.* APL Materials, 2013. **1**(1): p. 011002.
20. Bartel, C.J., et al., *Physical descriptor for the Gibbs energy of inorganic crystalline solids and temperature-dependent materials chemistry.* Nature Communications, 2018. **9**: p. 4168.
21. Linstrom, P.J. and W.G. Mallard, *The NIST Chemistry WebBook: A Chemical Data Resource on the Internet.* Journal of Chemical and Engineering Data, 2001. **5**: p. 5.
22. Nelson, L.J., et al., *Compressive sensing as a paradigm for building physics models.* Physical Review B, 2013. **87**: p. 035125.
23. Richards, W.D., et al., *Fluorination of Lithium-Excess Transition Metal Oxide Cathode Materials.* Advanced Energy Materials, 2018. **8**: p. 1701533.
24. Bianchini, M., et al., *The interplay between thermodynamics and kinetics in the solid-state synthesis of layered oxides.* Nature Materials, 2020. **19**: p. 1088-1095.
25. Bai, J., et al., *Kinetic Pathways Templated by Low-Temperature Intermediates during Solid-State Synthesis of Layered Oxides.* Chemistry of Materials, 2020. **17**: p. 9906-9913.
26. DeHoff, R., *Thermodynamics in Materials Science.* Taylor & Francis, 2006.
27. Janz, G.J., et al., *Physical Properties Data Compilations Relevant to Energy Storage.* U.S. Department of Commerce, 1978.
28. Miura, A., et al., *Observing and Modeling the Sequential Pairwise Reactions that Drive Solid-State Ceramic Synthesis.* Advanced Materials, 2021. **33**(24): p. 2100312.
29. Belsky, A., et al., *New developments in the Inorganic Crystal Structure Database (ICSD): accessibility in support of materials research and design.* Acta Crystallographica Section B, 2002. **B58**: p. 364-369.

30. Kononova, O., et al., *Text-mined dataset of inorganic materials synthesis recipes.* Scientific Data, 2019. **6**: p. 203.
31. Douglas, T.B. and J.L. Dever, *Lithium Fluoride: Heat Content from 0 to 900°, the Melting Point and Heat of Fusion.* Journal of the American Chemical Society, 1954. **76**(19): p. 4826-4829.
32. Zhong, P., et al., *Increasing Capacity in Disordered Rocksalt Cathodes by Mg Doping.* Chemistry of Materials, 2020. **32**: p. 10728-10736.
33. Clément, R.J., et al., *Short-Range Order and Unusual Modes of Nickel Redox in a Fluorine-Substituted Disordered Rocksalt Oxide Lithium-Ion Cathode.* Chemistry of Materials, 2018. **30**: p. 6495-6956.
34. Gan, Z. and R.R. Ernst, *An Improved 2D Magic-Angle-Turning Pulse Sequence for the Measurement of Chemical-Shift Anisotropy.* Journal of Magnetic Resonance, Series A, 1996. **123**(1): p. 140-143.
35. Hung, I., et al., *Isotropic High Field NMR Spectra of Li-Ion Battery Materials with Anisotropy >1 MHz.* Journal of the American Chemical Society, 2012. **134**(4): p. 1898-1901.
36. Ngatchou, P., A. Zarei, and A. El-Sharkawi. *Pareto Multi Objective Optimization*. in *Proceedings of the 13th International Conference on, Intelligent Systems Application to Power Systems*. 2005.
37. Narukawa, S., et al., *Anti-fluorite type Li6CoO4 , Li5FeO4 , and Li6MnO4 as the cathode for lithium secondary batteries.* Solid State Ionics, 1999. **122**: p. 59-64.
38. Federov, P.P. and A.A. Alexandrov, *Synthesis of inorganic fluorides in molten salt fluxes and ionic liquid mediums.* Journal of Fluorine Chemistry, 2019. **227**: p. 109374.
39. Sim, S.-J., et al., *Use of carbon coating on -LiNi0.8Co0.1Mn0.1O2 cathode material for enhanced performances of lithium-ion batteries.* Scientific Reports, 2020. **10**: p. 11114.
40. Pigliapochi, R., et al., *Structural Characterization of the Li-Ion Battery Cathode Materials LiTixMn2−xO4 (0.2 ≤ x ≤ 1.5): A Combined Experimental 7Li NMR and First-Principles Study.* Chemistry of Materials, 2018. **30**: p. 817-829.
41. Blasse, G., *The structure of some new mixed metal oxides containing lithium.* Journal of Inorganic and Nuclear Chemistry, 1963. **25**: p. 743-744.
42. Hardy, A., et al., *Preparation, proprietes cristallines et magnetiques de l'orthotitanate de manganese Mn2TiO4.* Comptes Rendus Hebdomadaires des Seances de l'Academie des Sciences, 1964. **259**: p. 3462-3465.
43. Chung, H., et al., *Experimental considerations to study Li-excess disordered rock salt cathode materials.* Journal of Materials Chemistry A, 2021. **9**: p. 1720.
44. Kitchaev, D.A., et al., *Design principles for high transition metal capacity in disordered rocksalt Li-ion cathodes.* Energy & Environmental Science, 2018. **11**: p. 2159.
45. Raccuglia, P., et al., *Machine-learning-assisted materials discovery using failed experiments.* Nature, 2016. **533**: p. 73-76.
46. Scheffee, R.S. and J.L. Margrave, *Vapor Pressure Equations for Species over Solid and Liquid LiF* The Journal of Chemical Physics, 1959. **31**: p. 1682.
47. McDermott, M.J., S.S. Dwaraknath, and K.A. Persson, *A graph-based network for predicting chemical reaction pathways in solid-state materials synthesis.* Nature Communications, 2021. **12**: p. 3097.
48. Aykol, M., J.H. Montoya, and J. Hummelshøj, *Rational Solid-State Synthesis Routes for Inorganic Materials.* Journal of the American Chemical Society, 2021. **143**: p. 9244-9259.

49. Kovnir, K., *Predictive Synthesis.* Chemistry of Materials, 2021. **33**: p. 4835-4841.
50. Moghadam, Y.S., et al., *Toward Better Stability and Reversibility of the Mn4+/Mn2+ Double Redox Activity in Disordered Rocksalt Oxyfluoride Cathode Materials.* Chemistry of Materials, 2021. **33**: p. 8235-8247.
51. Massiot, D., et al., *Modelling one- and two-dimensional solid-state NMR spectra.* Magnetic Resonance in Chemistry, 2001. **40**: p. 70-76.